

Datasheet of Photoplethysmography (PPG) and Accelerometer (ACC) Sensor

1. Overview

This work presents the design and evaluation of two autonomous wireless sensor nodes: a photoplethysmography (PPG) node and an accelerometer (ACC) node. Both sensor nodes share a common system architecture, including power management, microcontroller unit (MCU), and wireless communication, while differing only in the sensing front-end.

Each node is powered by a rechargeable coin-cell battery to ensure safe operation and stable supply voltages. A power multiplexer enables seamless switching between battery and USB power, allowing wired operation during programming and testing while maintaining autonomous battery-powered functionality during normal use.

An ESP32-C3 microcontroller is used as the central processing unit, providing sensor control, data acquisition, and Bluetooth Low Energy (BLE) wireless communication. Sensor data are transmitted wirelessly to a mobile device via BLE for real-time monitoring and data logging.

The PPG sensor node is designed for physiological monitoring through optical detection of blood volume changes, while the accelerometer node is intended for motion and activity sensing.

2. Features & Key Specifications

Table 1 Specifications of PPG

Category	Parameter to Record	Condition
Sampling	50Hz	Sensor sampling
Refresh	10s	Sending data
Optical	LED current	10–20 mA
Accuracy of SPO ₂	≈ 99%	Resting/exercise
Accuracy of Heart rate	> 60%/50%	Resting/exercise
Timing	Timestamp jitter	Continuous sampling
Rated voltage	~3.6V	Li-ion battery
Connection range	10m	Free air
Precision of SPO ₂	≈ ±1%	Resting/exercise
Precision of Heart Rate	≈ ±20%	Resting/exercise

Table 2 Specifications of ACC

Category	Parameter to Record	Condition
Sampling	100Hz	Sensor sampling
Noise (x, y, z)	(6.4%, 3.5%, 0.7%)	Scale error
Noise (x, y, z)	(0.16, -0.065, -0.02)	Zero offset
Motion	Rest/Moving	Change of acceleration
Precision	≈ ±5%	Multiple trials
Rated voltage	~3.6V	Li-ion battery
Connection range	1.5m	Free air
Accuracy	≈ 95%	static

3. Characterization methodology

3.1 PPG Characterization Method

Reference Device Comparison uses a commercial device (e.g. Apple Watch). For the same subject, the Device Under Test (DUT) and a commercial smartwatch (Apple Watch) are worn simultaneously to provide a practical reference for both heart rate (HR) and blood oxygen saturation (SpO₂). Two operating conditions are evaluated:

Resting state: the subject remains seated with arms relaxed while continuously recording 1 minute of HR data. SpO₂ is recorded during the same period (or as repeated spot readings if the reference device only provides intermittent SpO₂ updates).

Exercise state: the subject performs light exercise (e.g., walking or arm swinging) while continuously recording 1 minute of HR data. SpO₂ is recorded immediately after exercise (once the readings stabilise) and, if available, during the exercise period.

The DUT outputs (HR and SpO₂) are synchronously logged alongside the Apple Watch readings and compared point-by-point (for HR) and time-matched (for SpO₂). Accuracy against the reference is quantified using metrics such as Mean Absolute Error (MAE), and the percentage of samples within a specified tolerance band (e.g., ±5 bpm for HR and ±2–3% for SpO₂). Testing both resting and exercise conditions assesses performance under ideal conditions and in the presence of motion artefacts, aligning with real-world use. In addition, precision is assessed via repeated measurements on multiple participants (e.g., several subjects, multiple repeated trials per subject under the same condition).

3.2 Bluetooth Range Characterization Method

To measure the on-board Bluetooth communication range, a connection-based distance verification method is employed.

The DUT is connected to a smartphone via Bluetooth. While maintaining the Bluetooth connection, the distance between the DUT and the central device is gradually increased. The ability to successfully maintain the Bluetooth connection at different distances is recorded. The maximum Bluetooth connection distance is defined as the farthest distance at which the device can still successfully establish or maintain a connection.

The rationale for this verification approach stems from Bluetooth range being the most intuitive wireless performance metric for users. By increasing distance, we can objectively evaluate the system's communication capability in real-world environments and establish clear performance boundaries.

3.3 ACC Static Characterization Test Method

To measure accelerometer performance, a controlled variable measurement method is employed. The device is placed stationary on a horizontal surface, with each of its six faces oriented downward in turn (corresponding to the $\pm X$, $\pm Y$, and $\pm Z$ directions). For each orientation, accelerometer output data is recorded for 20 seconds, and the average value is calculated. The theoretically expected value for the axis aligned with the direction of gravity should be close to ± 1 g ($\approx 9.81 \text{ m/s}^2$); the accelerations for the other two axes should be close to 0 g. By comparing measured values with theoretical values, the offset error and static accuracy for each axis are evaluated.

This verification protocol comprises six static gravity tests, enabling accelerometer characterization without additional equipment. Utilizing gravity as a known reference effectively evaluates the accelerometer's zero bias and proportional error.

4. Hardware Design of ACC & PPG

4.1 Overview of Hardware Structure

The PPG node and the ACC node are implemented as two separate autonomous sensor boards. The entire structure block diagram of hardware is shown in Figure 1.

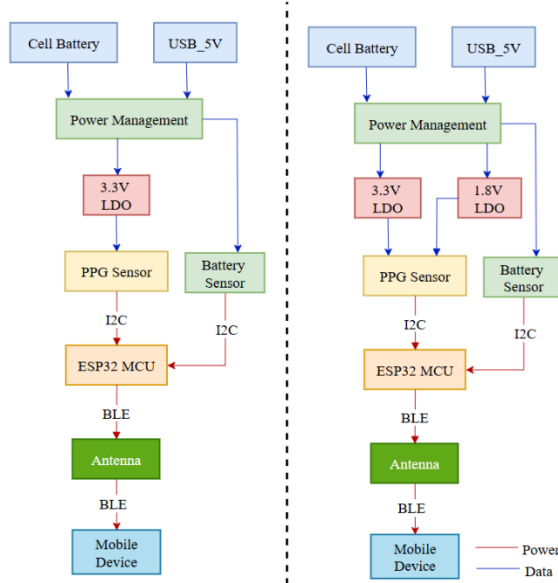


Figure 1 Flow Chart of ACC, PPG

4.2 Power Management

The power management subsystem is designed to support autonomous battery operation while allowing safe USB-powered programming and debugging. The architecture ensures battery protection, controlled power switching, inrush current limitation, and stable voltage regulation for sensitive digital and analogue components.

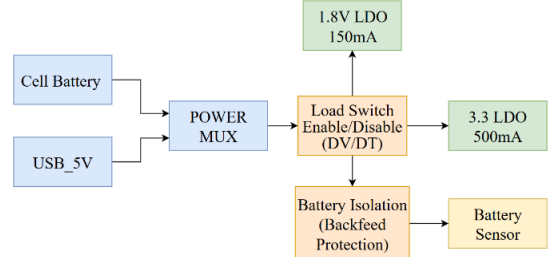


Figure 2 Block Diagram of Power Management

4.2.1 Battery Protection (DW01 + FS8205A)

The DW01 battery protection IC continuously monitors the cell voltage and current. In the event of over-voltage, under-voltage, over-current, or reverse connection, the DW01 asserts gate control signals (G1 and G2) to the FS8205A dual back-to-back NMOS switch, disconnecting the battery from the system. This prevents battery damage and protects downstream circuitry under fault conditions.

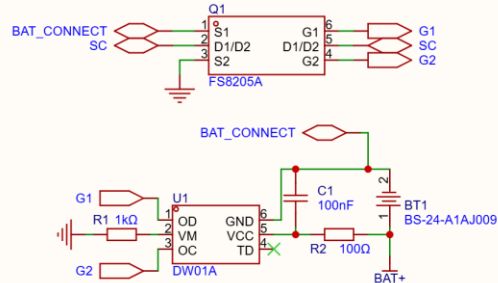


Figure 3 DW01 Battery Protection Circuit

4.2.2 USB Interface Protection (USB Type-C)

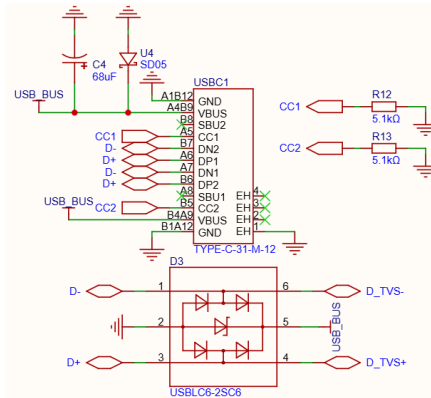


Figure 4 Type C for USB_BUS

To protect the system against electrostatic discharge (ESD), transient voltage suppressor (TVS) diodes are placed on both the USB power and data lines. This ensures that ESD events occurring at the USB connector do not propagate into the system and damage sensitive components.

4.2.3 Power Source Selection (TPS2116 Power Mux)

A power multiplexer is used to select between battery and USB power sources. To prevent reverse current and back-feeding between battery and USB 5V at Mode pin, each input path includes a diode. An NMOS-controlled LED provides visual indication of USB power presence. A series resistor is placed between the USB 5 V rail and the NMOS gate to slow the gate charging rate, reducing stress on the device and improving long-term reliability.

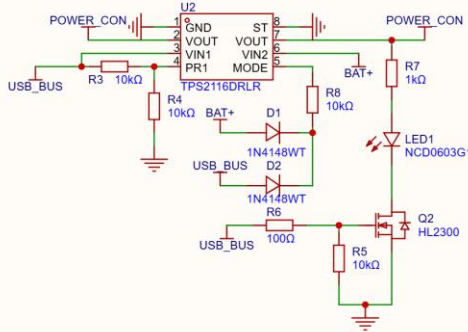


Figure 5 TPS2116 Power Mux

4.2.4 Inrush Limiting (TPS22992)

The TPS22992 load switch controls the system power rail and implements a controlled soft-start using the dv/dt. This limits the inrush current during power-up, preventing excessive current draw from the battery.

Given a total system capacitance of approximately 148.5 μF and a maximum allowable battery current of 200 mA, the required minimum rise time is calculated as:

$$t_{on} = \frac{C_L * VDD}{A_{max}} \approx 2.45\text{ms} \quad (1)$$

To provide sufficient margin, a rise time of 6.13 ms is selected, resulting in a maximum inrush current of approximately 80 mA, well below the battery limit.

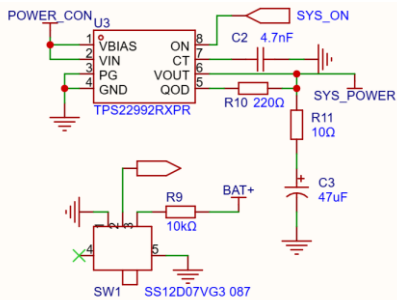


Figure 6 TPS22992 System Power Switch

CT Capacitor	VIN = 5 V	VIN = 3.3 V
0 pF	147 μs	113 μs
220 pF	426 μs	297 μs
1000 pF	1430 μs	962 μs
4700 pF	6130 μs	4090 μs

Table 3 Rising time for different CT Capacitor [1]

4.2.5 Voltage Regulation (3.3 V and 1.8 V LDOs)

Low-dropout regulators generate the required 3.3 V and 1.8 V supply rails for the MCU and sensors. Different output capacitances are selected to optimize transient response and reduce output ripple, ensuring stable operation under varying load conditions.

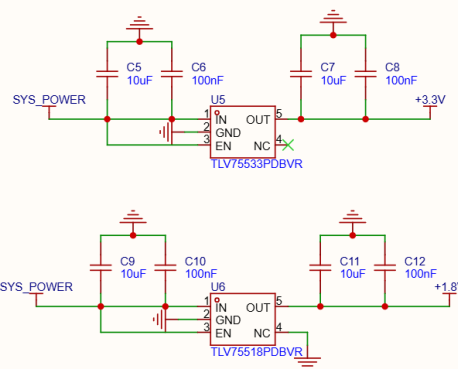


Figure 7 3.3V and 1.8V LDO for the System

4.2.6 Battery Monitor Protection via PMOS Auto Control
The MAX17048 battery monitor operates within a recommended supply voltage range of 2.5 V to 4.5 V. When USB power is present, the system voltage may rise to 5 V, exceeding the recommended limit. To prevent damage and long-term degradation, a PMOS switch automatically disconnects the battery monitor during USB-powered operation.

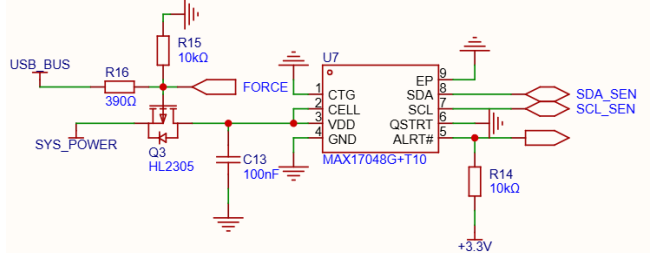


Figure 8 PMOS Auto Control with Battery Monitor

Electrical Characteristics

($VDD = 2.5\text{V}$ to 4.5V , $T_A = -20^\circ\text{C}$ to $+70^\circ\text{C}$, unless otherwise noted. Typical values are at $T_A = +25^\circ\text{C}$). (Note 1)

PARAMETER	SYMBOL	CONDITIONS	MIN	TYP	MAX	UNITS
Supply Voltage	V_{DD}	(Note 2)	2.5	4.5	4.5	V
Fuel-Gauge SOC Reset (VRESET Register)	V_{RST}	Configuration range, in 40mV steps Trimmed at 3V	2.28	3.48	3.48	V
			2.85	3.0	3.15	V

Table 4 Recommend Supply Voltage Range [2]

4.3 MCU, Sensor and Interface Design

4.3.1 MCU Design

The ESP32-C3 integrates both digital and analogue subsystems, requiring careful power supply decoupling. Local 100 nF and 10 μF capacitors are placed close to the supply pins to suppress high- and low-frequency noise. Ferrite beads are used to isolate digital and analogue supply paths, reducing switching noise coupling and improving power integrity.

Due to the limited number of available GPIOs on the ESP32-C3, certain default functions are reassigned. USB is used for debugging instead of JTAG, allowing JTAG pins to be repurposed as GPIO or I²C interfaces.

To enable long-term autonomous operation, the MCU enters sleep mode during inactivity. The system can be awakened either wirelessly via BLE or manually using a hardware wake-up button, significantly reducing average power consumption.

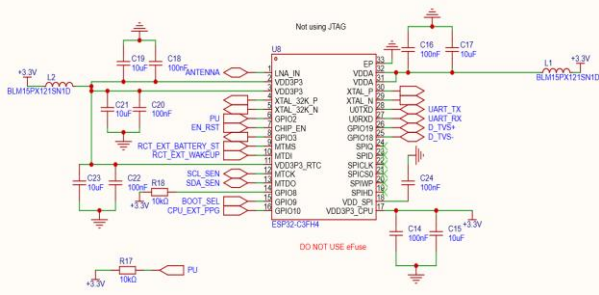


Figure 9 ESP32C3 MCU Design

4.3.2 Crystal Oscillator for ESP32-C3

A 40 MHz crystal oscillator is used as the main system clock, providing stable timing for MCU operation, wireless communication, and peripheral control. A secondary 32.768 kHz crystal is used to support the RTC domain, enabling low-power sleep modes and timed wake-up events.

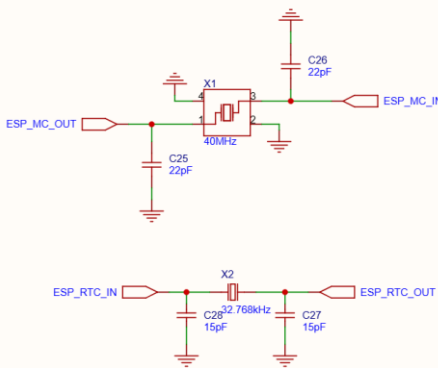


Figure 10 Crystal Oscillator for ESP32C3

4.3.3 User Interaction and Control

The ESP32-C3 requires a dedicated enable (EN) pin for hardware reset and a boot configuration pin to select between programming mode and normal operation. To accommodate these requirements while maintaining system functionality, a control interface consisting of two buttons and two switches is implemented.

These controls correspond to:

- MCU reset button
- MCU wake-up button
- Boot mode selection switch
- PMOS control switch

To ensure stable system startup, the RC charging time on the EN pin is designed to be longer than the specified stabilisation time t_{stable} . This prevents unintended resets or unstable behaviour during power-up.

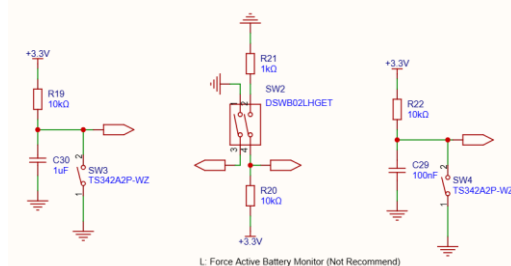


Figure 11 Interaction for ESP32C3

The timing diagram illustrates the controlled rise of the EN pin voltage, ensuring the MCU exits reset only after the power supply has stabilised.

The PMOS control switch is used during USB-powered debugging to temporarily enable the battery monitoring circuit. This allows verification of I²C communication and battery sensor functionality without permanently powering the battery monitor during USB operation.

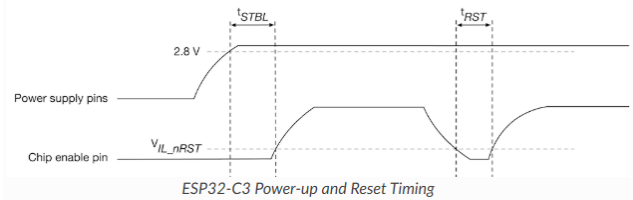


Figure 12 Time Diagram of EN Pin [3]

Attention

- CHIP_EN must not be left floating.
- To ensure the correct power-up and reset timing, it is advised to add an RC delay circuit at the CHIP_EN pin. The recommended setting for the RC delay circuit is usually $R = 10\text{ k}\Omega$ and $C = 1\text{ }\mu\text{F}$. However, specific parameters should be adjusted based on the characteristics of the actual power supply and the power-up and reset timing of the chip.

Figure 13 Attention for ESP32C3 Power-up [3]

4.3.4 I²C Pull-Up Resistor Power Switch

For MAX-series I²C sensors, pulling both SDA and SCL lines low places the sensor into sleep mode. To exploit this behavior and minimize power consumption, a dedicated power switch controls the supply to the I²C pull-up resistors. When the switch is disabled, the pull-up resistors lose the supply and the I²C lines are actively discharged to ground using the Quick Output Discharge (QOD) feature of the TPS22992. This ensures a fast transition to the sensor sleep state and guarantees defined logic levels during low-power operation.

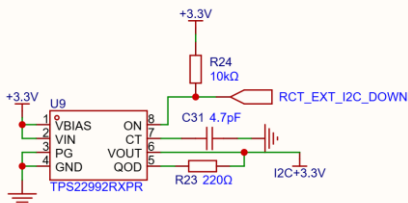


Figure 14 I2C Pull Up Resistor Power Switch

4.3.5 Antenna Design

A chip antenna is used for BLE communication. According to the antenna datasheet, a π -type matching network is required to ensure impedance matching and stable RF performance. A C-L-C configuration is implemented to allow tuning and optimization of antenna matching during testing.

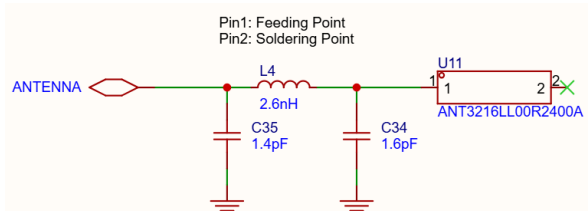


Figure 15 ESP32C3 ANTENNA

4.3.6 PPG Sensor Design

The PPG sensor includes high-current LED drivers and noise-sensitive analogue circuitry. To minimize interference, the power ground (PGND) used by the LED drivers is separated from the digital ground (GND) and connected at a single point. This star-ground approach reduces ground bounce and noise coupling.

A ferrite bead is placed in series with the 3.3 V supply to the LED driver to suppress high frequency switching noise. The 1.8 V supply is used exclusively by the PPG circuitry and does not require additional isolation.

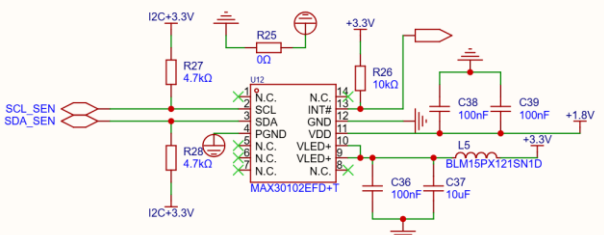


Figure 16 PPG Sensor Circuit

4.3.7 ACC Sensor Design

The accelerometer is powered from the regulated 3.3 V supply and communicates with the MCU via a digital interface. Decoupling capacitors are placed close to the sensor to ensure supply stability and reduce susceptibility to noise.

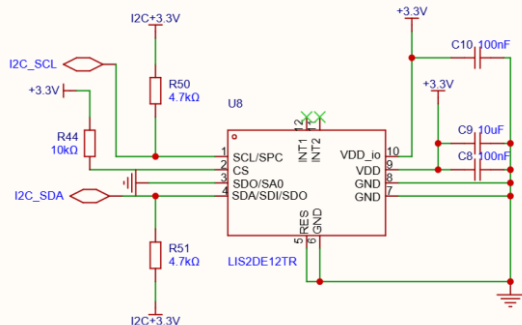


Figure 17 ACC Sensor Circuit

4.4 PCB Design and Consideration

4.4.1 PCB Diagram of PPG & ACC (Top & Bottom Layer)

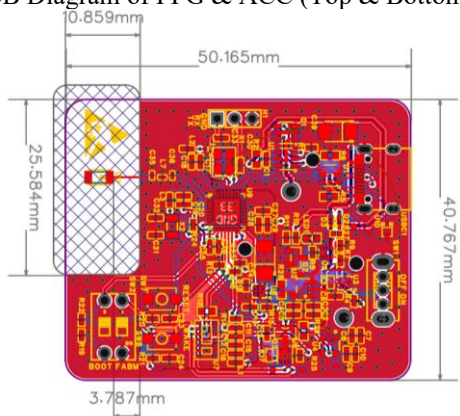


Figure 18 PPG Sensor Node Top Layer

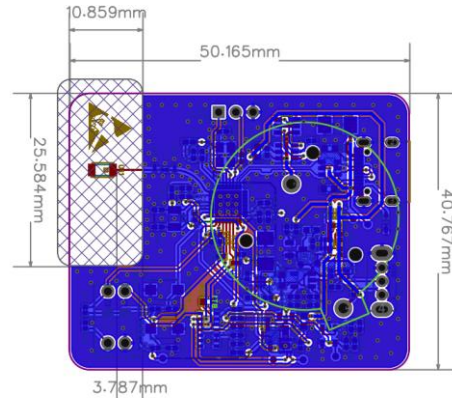


Figure 19 PPG Sensor Node Bottom Layer

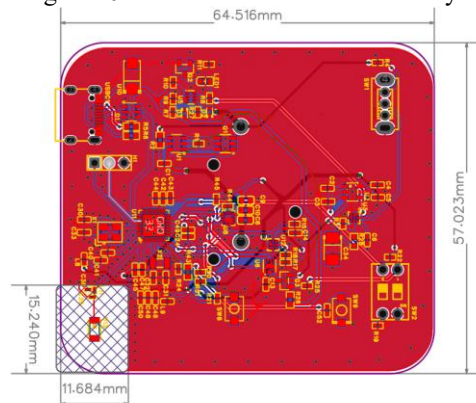


Figure 20 – ACC Sensor Node Top Layer

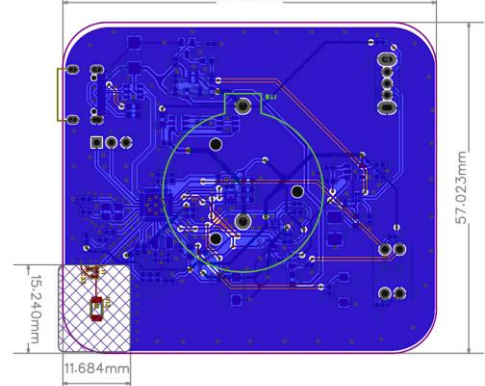


Figure 20 ACC Sensor Node Bottom Layer

4.4.2 PCB Design Considerations

For the PCB layout, particular attention is given to high-speed USB differential routing and RF antenna performance, as both are highly sensitive to impedance control and layout constraints.

Texas Instruments
www.ti.com

A Device Layout Parameters

Parameter	MIN	TYP	MAX	Unit
USB2.0 Tracelength (total)			4000	12000
Skew within any USB2.0 differential pair			50	Mils
USB2.0 DP/DM pair differential impedance	81	90	99	Ω

Figure 21 USB2.0 Trace Requirement [4]

USB 2.0 high-speed data transmission requires controlled differential impedance and length matching to maintain signal integrity. The differential pair is routed as a tightly

coupled pair with consistent geometry along the entire path to minimize reflections and common-mode noise.

The USB differential pair is designed for a target differential impedance of 90Ω . A coplanar differential impedance model is adopted, as copper pouring on the top layer is required to reduce external interference. Using the JLC7628 stack-up, a trace width of 8 mil and a spacing of 5 mil are selected to achieve the target impedance.

JLC7628(Finished thickness 1.58mm ± 10%)		JLC041W-B-3313A(Special/Finished thickness 1.58mm ± 10%)		JLC041W-B-702B(Standard/Finished thickness 1.58mm ± 10%)			
Impedance (Ω)	Type	Signal Layer	Top Ref	Bottom Ref	Trace Width	Trace Spacing	Impedance trace to copper
z0	Coplanar Differential Pair	L1	/	L2	7.000	5.0000	10.000
Layer	Material				Thickness (mil)	Thickness (mm)	
L1	Outer Copper Weight				1.38	0.0350	
Prepreg	702B, RC 49%, 8.6 mil					0.2104	
L2	Inner Copper Weight				0.60	0.0152	
Core	11mm HfNO ₂ with copper				41.93	1.0850	
L3	Inner Copper Weight				0.60	0.0152	
Prepreg	702B, RC 49%, 8.6 mil				8.28	0.2104	
L4	Outer Copper Weight				1.38	0.0350	

Figure 22 Impedance Calculation for Differential Pair [5]

Length mismatch in differential routing can introduce current skew and degrade signal quality. To minimize timing skew between the differential signals, length compensation is applied to the USB data lines. The length mismatch is kept within 50 mil, which is within the tolerance specified by the USB 2.0 standard.

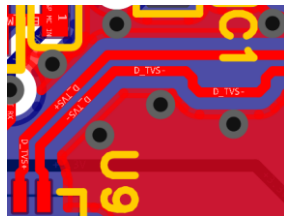


Figure 23 Differential Pair Trace Length Compensation

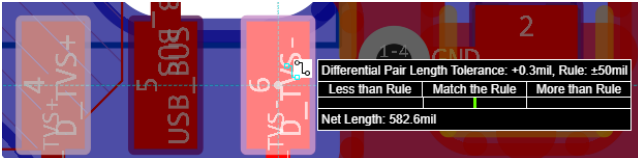


Figure 24 Current Skew for Differential Pair Trace Length

4.4.3 Antenna Design Considerations

For the chip antenna, maintaining a clear keep-out area around the antenna is critical for efficient radiation. Copper, components, and signal traces are excluded from this region to prevent detuning and signal attenuation.

Compared to the reference evaluation board, the PPG PCB provides a larger antenna clearance area, with edge lengths of 25.584 mm and 10.859 mm. In addition, the distance between the chip antenna and the ground plane is increased to 3.787 mm, compared to 2 mm on the evaluation board, reducing ground coupling and improving radiation efficiency.

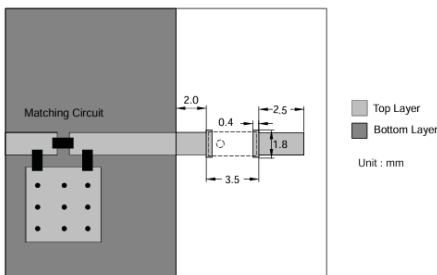


Figure 25 Antenna Clearance Between Ground Planes [6]

These PCB layout techniques ensure reliable high-speed data communication and stable wireless performance while minimizing noise coupling and signal degradation.

5. Signal Processing Approach

5.1 Firmware-level System Overview

Both the photoplethysmography (PPG) sensor node and the accelerometer (ACC) sensor node are implemented on the same ESP32 MCU platform, each running dedicated firmware for real-time data acquisition, signal conditioning, feature extraction, and wireless transmission. Each firmware instance is structured around a single-threaded main loop with predictable timing, using I²C for sensor communication and Bluetooth Low Energy (BLE) for low-latency data delivery to external devices.

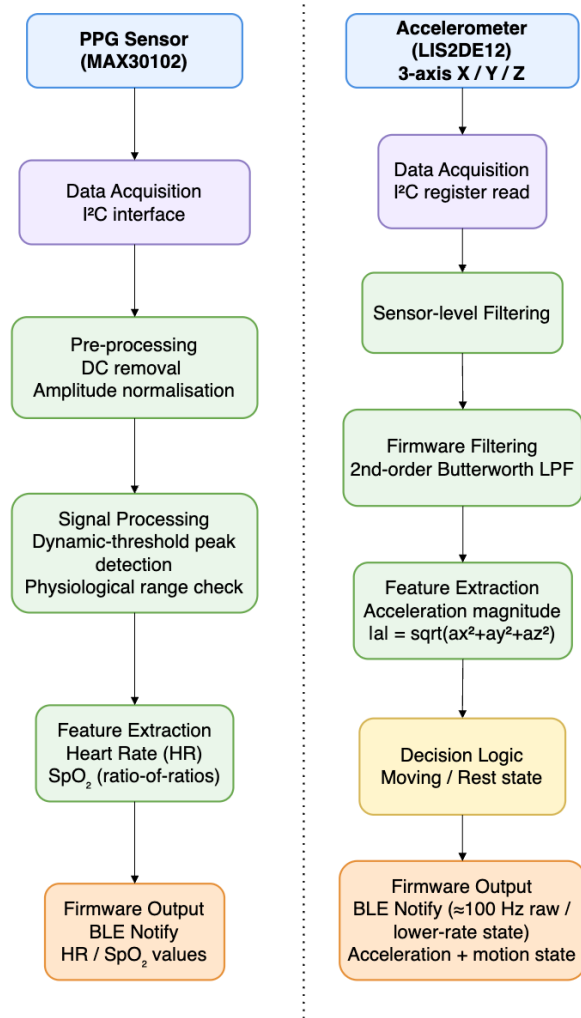


Figure 26 Firmware System of ACC, PPG

5.2 Firmware Implementation and Data Acquisition

Both accelerometer and photoplethysmography sensor data are transmitted over the I²C bus and configured by the firmware. Data acquisition is performed at stable sampling rates to ensure temporally contiguous data, providing a reliable basis for subsequent signal processing.

For motion detection, the LIS2DE12 accelerometer is configured via direct register access. The device operates at

a 100 Hz data output rate with all three axes enabled, employing high-resolution mode and a ± 2 g full-scale range to maximize sensitivity for human motion detection. An internal high-pass filter is enabled at the sensor level to attenuate gravity components before data transmission to the microcontroller. Raw acceleration samples are read as 12-bit signed values, stored left-aligned in 16-bit registers, and converted to physical g units. Sampling intervals are controlled by fixed delays, generating a stable and predictable data stream.

For PPG, the MAX30102 photoplethysmography sensor is accessed via manufacturer drivers, configured for dual-wavelength operation with RED and IR LEDs. Operating at 50Hz sampling rate, the sensor enhances signal quality through internal sampling averaging. PPG data per channel is stored in fix-length buffered array containing 50 samples, corresponding to approximately one second's time window. Data acquisition employs a blocking mode at the buffer level, ensuring the continuous samples required for physiological signal analysis. The moderate sampling rate and finite buffer capacity maintain overall firmware responsiveness.

This unified firmware-level acquisition strategy enables heterogeneous sensors with differing timing requirements to coexist within the same system, whilst maintaining deterministic sampling behavior and ensuring compatibility with downstream signal processing pipelines.

5.3 Signal Conditioning and Filtering

5.3.1 Accelerometer signal conditioning:

After conversion from raw integer samples to floating-point acceleration values expressed in units of g, each accelerometer axis is processed by a second-order Butterworth low-pass infinite impulse response (IIR) filter. The filter is designed for a sampling frequency of $f_s=100$ Hz with a cut-off frequency of approximately $f_c = 5$ Hz, corresponding to the dominant frequency range of human motion.

The digital filter can be expressed in the standard biquad difference equation form:

$$y[n] = b_0x[n] + b_1x[n - 1] + b_2x[n - 2] - a_1y[n - 1] - a_2y[n - 2] \quad (2)$$

where $x[n]$ and $y[n]$ denote the input and output samples respectively, and the coefficients b_i and a_i are selected to realize a maximally flat Butterworth magnitude response in the passband. This filtering stage effectively attenuates high-frequency sensor noise and mechanical vibration while preserving motion-relevant dynamics.

The filtered three-axis acceleration components are subsequently combined into a scalar magnitude:

$$|a[n]| = \sqrt{a_x^2[n] + a_y^2[n] + a_z^2[n]} \quad (3)$$

which provides an orientation-independent representation of motion intensity. This formulation removes sensitivity to device orientation and allows motion detection to be based solely on the overall acceleration energy.

To classify the motion state, a threshold-based decision rule is applied to the acceleration magnitude:

$$|a[n]| \geq \gamma \quad (4)$$

where γ is an empirically selected threshold. To improve robustness against noise-induced fluctuations, a debounce mechanism is implemented, requiring the threshold condition to be satisfied for a predefined number of consecutive samples before the system state transitions between *moving* and *stationary*. This approach reduces spurious detections caused by transient disturbances or residual sensor noise.

5.3.2 PPG signal conditioning:

PPG signal conditioning is performed on buffered RED and IR optical samples acquired over a fixed temporal window of approximately one second. Let $s[n]$ denote the raw PPG signal within a buffer of length N. A DC removal step is applied by subtracting the mean value of the buffer:

$$s_{AC}[n] = s[n] - \frac{1}{N} \sum_{k=0}^{N-1} s[k] \quad (5)$$

thereby isolating the pulsatile AC component associated with the cardiac cycle and suppressing slow-varying baseline offsets.

For heart-rate estimation, the conditioned waveform is analysed using a dynamic-threshold peak detection algorithm. The detection threshold is defined as a fraction of the signal's standard deviation:

$$\theta = \alpha \cdot \sigma, \quad \sigma = \sqrt{\frac{1}{N} \sum_{k=0}^{N-1} s_{AC}^2[n]} \quad (6)$$

where α is an empirically chosen scaling factor. A peak is detected when the signal crosses the threshold in the positive direction, subject to a refractory condition that prevents multiple detections within a single cardiac cycle.

Detected peak indices $\{n_i\}$ are used to estimate the inter-beat interval:

$$T_{RR} = \frac{1}{(M-1)f_s} \sum_{i=2}^M (n_i - n_{i-1}) \quad (7)$$

where f_s is the sampling frequency and M is the number of valid peaks. The heart rate is then computed as:

$$HR (\text{bpm}) = \frac{60}{T_{RR} (\text{s})} \quad (8)$$

Physiological plausibility constraints are applied to reject implausible values.

This adaptive thresholding approach improves robustness to variations in signal amplitude caused by finger pressure, skin tone, or optical coupling, and allows reliable heart-rate estimation under varying measurement conditions.

In addition to heart-rate estimation, blood oxygen saturation (SpO_2) is estimated from the RED and IR PPG channels using the widely adopted ratio-of-ratios method. Let, AC_{red} , DC_{red} and denote the AC and DC components of the red and infrared signals, respectively, extracted from the buffered PPG samples.

The ratio-of-ratios is defined as:

$$R = \frac{AC_{red}/DC_{red}}{AC_{IR}/DC_{IR}} \quad (9)$$

This ratio exploits the wavelength-dependent absorption characteristics of oxygenated and deoxygenated haemoglobin. The estimated SpO_2 is then obtained through an empirically calibrated mapping:

$$\text{SpO}_2 = f(R) \quad (10)$$

Where $f(\cdot)$ is a monotonic function determined through experimental calibration. In this implementation, the mapping is provided by the vendor-supplied algorithm library.

While this approach does not yield clinical-grade accuracy, it provides a computationally efficient and widely accepted method for estimating relative oxygen saturation trends in wearable sensing applications.

5.4 Feature Extraction and Physiological Metrics

Heart Rate and Blood Oxygen Saturation Estimation:

Based on the signal conditioning and peak detection process described in Section 3.3, heart rate (HR) is estimated from the infrared PPG channel using the time interval between consecutive valid pulse peaks. The resulting inter-beat interval is converted to beats per minute, with physiologically plausible values retained to exclude unreasonable readings caused by noise or motion artefacts.

Blood oxygen saturation (SpO_2) is estimated using the ratio method proposed in Section 3.3, based on the RED and IR PPG channels. The calculated ratio is mapped to an SpO_2 estimate via an empirically calibrated function from the vendor's algorithm library. While this method lacks clinical-grade accuracy, it reliably estimates relative oxygen saturation values, making it suitable for wearable sensing demonstrations and comparative analyses.

To enhance transparency and adjustability at the firmware level, this system prioritizes heart rate estimates derived from a custom peak detection algorithm over outputs provided by library files. Conversely, SpO_2 estimation continues to utilize the vendor's validated implementation. Motion-related features extracted from the accelerometer signal.

Based on the filtered triaxial accelerometer signals described in Section 3.3, motion data is extracted, including acceleration along the X, Y, and Z axes, orientation-independent acceleration magnitude, and a binary motion state indicating movement or rest.

The binary motion state generates a description of user activity through threshold processing and debouncing logic. Collectively, these motion data constitute contextual information that aids in assessing the user's motion state and intensity.

5.5 Wireless Data Output and Update Rate

Extracted metrics (heart rate and blood oxygen saturation) alongside motion characteristics derived from the ACC are transmitted wirelessly via Bluetooth Low Energy (BLE) using notification-enabled functionality. Data is encoded in compact UTF-8 text messages, facilitating real-time verification during demonstrations and streamlining debugging procedures.

To constrain wireless bandwidth usage and reduce power consumption, derived metrics employ a rate-limiting

mechanism, transmitting at approximately 1Hz, which is independent of the raw sensor sampling rate. This decoupled design ensures stable wireless communication while maintaining sufficient temporal resolution for monitoring physiological trends.

Furthermore, the firmware periodically interrogates the battery monitor (MAX17048) integrated onto the shared I²C bus. Battery voltage and charge status are transmitted via dedicated Bluetooth Low Energy characteristics, enabling energy awareness during extended measurement sessions.

5.6 Algorithm Delays and Limitations

The firmware and signal processing workflow employed introduce varying delays to the sensors. Accelerometer outputs undergo near-real-time processing, with delays primarily influenced by digital filtering, typically maintained within tens of milliseconds. In contrast, heart rate and blood oxygen saturation estimates exhibit delays equivalent to buffer duration and data acquisition time (≈ 1 seconds), reflecting the requirement for temporal context in physiological signal analysis.

System limitations include PPG measurements being susceptible to motion artefacts, ambient light interference, and variations in sensor-skin coupling; accelerometer-derived features being dependent on sensor orientation and mounting configuration. Nevertheless, this architecture delivers stable, low latency estimates suitable for wearable sensing demonstrations and comparative evaluations.

6. Result Error Analyse

Heart rate (HR) and SpO_2 were compared with a smartwatch reference under rest and light exercise. In our tests, SpO_2 achieved an accuracy of $\approx 99\%$ with a precision of $\approx \pm 1\%$ across conditions as recorded in Table 1. HR performance was more affected by motion, with accuracy $>60\%$ at rest and $>50\%$ during exercise, and an overall precision of $\approx \pm 20\%$, which is consistent with motion artefacts distorting the PPG waveform and reducing measurement stability.

The accelerometer was characterised using the six-orientation static gravity test. The dominant errors were axis-dependent scale-factor mismatch and zero-g offset, with measured scale error of (6.4%, 3.5%, 0.7%) and zero offset of (0.16, -0.065, -0.02) for the (x, y, z) axes. Overall static accuracy was $\approx 95\%$, and repeatability/precision across trials was $\approx \pm 5\%$ as shown in Table 2.

To improve HR robustness under motion, the PPG processing can be made motion-aware by using the accelerometer magnitude as a quality indicator: when strong motion is detected, HR updates are held or the detection threshold is tightened to reduce false peaks. Further improvement could be achieved by adding a simple band-pass filter around the cardiac band and/or using ACC-assisted artefact suppression, which directly targets the motion components that dominate the HR error.

Reference:

- [1] Texas Instruments, *TPS22992x 5-V, 8.7-mΩ, 6-A Load Switch With Adjustable Rise Time*, Datasheet, SLVSFT0A, Rev. A, Dec. 2021.
- [2] Maxim Integrated, *MAX17048/MAX17049 3μA 1-Cell/2-Cell Fuel Gauge with ModelGauge*, Datasheet, 19-6171, Rev. 7, Nov. 2016
- [3] Espressif Systems, “Schematic Checklist - ESP32-C3,” *ESP Hardware Design Guidelines* (online documentation). Accessed: 15 Dec. 2025.
- [4] Texas Instruments, *High-Speed Interface Layout Guidelines*, Application Report, SPRAAR7J, Feb. 2023.
- [5] JLCPCB, “JLCPCB Impedance Calculator,” *JLCPCB* (online tool/webpage). Accessed: 15 Dec. 2025.
- [6] Pulse Electronics (Larsen Antennas), *3216 2.4G Chip Antenna*, Datasheet, Part No. ANT3216LL00R2400A, Version 1, Oct. 13, 2020